FULL PAPER

Plasmonic-Induced Photon Recycling in Metal Halide Perovskite Solar Cells

Michael Saliba, Wei Zhang, Victor M. Burlakov, Samuel D. Stranks, Yao Sun, James M. Ball, Michael B. Johnston, Alain Goriely, Ulrich Wiesner, and Henry J. Snaith*

Organic–inorganic metal halide perovskite solar cells have emerged in the past few years to promise highly efficient photovoltaic devices at low costs. Here, temperature-sensitive core–shell Ag@TiO$_2$ nanoparticles are successfully incorporated into perovskite solar cells through a low-temperature processing route, boosting the measured device efficiencies up to 16.3%. Experimental evidence is shown and a theoretical model is developed which predicts that the presence of highly polarizable nanoparticles enhances the radiative decay of excitons and increases the reabsorption of emitted radiation, representing a novel photon recycling scheme. The work elucidates the complicated subtle interactions between light and matter in plasmonic photovoltaic composites. Photonic and plasmonic schemes such as this may help to move highly efficient perovskite solar cells closer to the theoretical limiting efficiencies.

1. Introduction

Perovskite, named after the Russian mineralogist Lev Perovski, is the designation given to any material adopting the crystal structure of calcium titanate (CaTiO$_3$), generally expressed as ABX$_3$. One subclass of perovskites where A is an organic cation, B a divalent metal, and X a halogen (or a mixture thereof), are solution-processable organic–inorganic metal halide perovskites such as methylammonium lead triiodide (CH$_3$NH$_3$PbI$_3$) first synthesized by Weber et al. in 1978.[1] This was employed in photovoltaic applications for the first time in a liquid electrolyte based dye sensitized solar cell (DSSC) architecture by Miyasaka et al. with power conversion efficiencies (PCEs) up to 3.8%.[2,3]

Efficiencies then exhibited a step-change improvement by substituting the liquid electrolyte with a solid state hole transporting material (HTM), 2,2′,7,7′-tetrakis-(N,N-di-p-methoxyphenylamine)9,9′-spirobifluorene (Spiro-OMeTAD).[4,5] By replacing the mesoporous titania scaffold, a crucial element in the traditional DSSCs, with alumina[5,6] or by removing the HTM,[7] the perovskite was shown to support charge-transport of electrons and holes, respectively. Very high internal quantum efficiencies were also observed where the mesoporous structure was discarded completely, reverting to a conventional thin-film solar cell architecture[6] or so-called planar heterojunction solar cell. Moreover, using a perovskite prepared from a mixed halide precursor[5] has enabled an early development of thin-film architectures due to advantageous film crystallization leading to high charge mobility[8] and long carrier diffusion length exceeding 1 µm.[8–11] To date, device efficiencies close to 20% have been achieved through materials design and optimization of processing techniques.[4,7,12–36] Further improvements are still likely through enhanced electronic properties of the crystalline perovskite thin films and the interfaces with the p- and n-type charge collection layers.

In order to reach the maximum performance, optical management will also be required. One strategy is to optically engineer the device to maximize light coupling into the active layer. This can be achieved through utilizing plasmonic effects, i.e., collective excitations of the surface electron gas on metallic structures by light with wavelengths many times larger than the object itself.[3,37–40] Traditionally, the focus has been on increasing the light harvesting efficiency, tuning color, or extending the absorption of the solar spectrum. However, this task is very challenging and to our knowledge only a few examples exist where plasmonic effects show an unambiguous photovoltaic enhancement, translating to an improved absorption or external quantum efficiency.[41–43] In our previous work, we incorporated plasmonic gold-silica core–shell nanoparticles (NPs) in the alumina scaffold of perovskite solar cells[44] resulting in an enhanced short-circuit current. However, this could not be attributed to increased light absorption. Rather, we presented data consistent with an increased ionization ratio of photoexcited electron–hole pairs.[44]

Gold is a well-known plasmonic material and has been intensively studied for a plethora of applications.[45–49]

Dr. M. Saliba, Dr. W. Zhang, Dr. S. D. Stranks,
Dr. J. M. Ball, Prof. M. B. Johnston, Prof. H. J. Snaith
Department of Physics
University of Oxford
Clarendon Laboratory
Parks Road, Oxford OX 1 3PU, UK
E-mail: h.snaith1@physics.ox.ac.uk
Dr. V. M. Burlakov, Prof. A. Goriely
Mathematical Institute
University of Oxford
Woodstock Road, Oxford OX 2 6GG, UK
Dr. Y. Sun, Prof. U. Wiesner
Department of Materials Science and Engineering
Cornell University
Ithaca, NY 14853, USA

However silver is a promising alternative for plasmonic applications because of its high quality factor (see Figure S1 in the Supporting Information) over a broad spectral range, outperforming most metals.[50,51] Moreover, the synthesis of silver NPs is inexpensive via wet chemistry procedures leading to many possible shapes and sizes, like triangles, cubes, stars, rods, and the obtained material can be deposited on substrates with relative ease due to self-assembly properties, allowing a myriad of optical properties to be investigated.[52] In addition, for large-scale photovoltaic applications, it is of great importance to reduce the material cost and silver is thus a better choice than gold. Although silver is of great scientific and industrial interest, it is chemically and thermally less stable than gold or other metals which limits its applicability in photovoltaics whenever high-temperature processing is involved.[53–57] This imposes an inherent difficulty, for example, in enhancing DSSCs where the mesoporous TiO_2 layer needs to be sintered at 500 °C.

Here, we successfully incorporate core–shell silver-titania nanoparticles ($Ag@TiO_2$) in organic–inorganic perovskite solar cells through a low-temperature processing.[6] By optimizing the concentration of $Ag@TiO_2$ in the active layer of the device, we observe a significant enhancement in the like-to-like performance delivering a power conversion efficiency of 16.3%. We propose a mechanism for the photocurrent improvement and develop a theoretical model in which the highly polarizable metallic nanoparticles increase the optical pathlength by acting as antennas for light reemitted from radiative recombination

of electron–hole pairs. This study opens the door to investigate the effect of plasmonic silver nanomaterials in low-temperature processed solar cells or other optoelectronic devices such as LEDs and lasers.

2. Results and Discussion

We start with the morphology study and optical characterization of the synthesized $Ag@TiO_2$ NPs. **Figure 1**a shows a cross sectional SEM image of a typical meso-superstructured perovskite solar cell (MSSC) used in this study. A 50 nm thick TiO_2 compact layer sits on top of an electron collecting fluorine-doped tin oxide (FTO) electrode, followed by an insulating Al_2O_3 scaffold. This scaffold is infiltrated and capped by perovskite, which forms the photoactive layer in which electrons and holes are generated and separated under solar irradiation. The holes are transported through the HTM (Spiro-OMeTAD) and collected at the silver electrode. The as-synthesized $Ag@TiO_2$ NP is relatively uniform in particle size as shown by TEM image in Figure 1b. The silver core size is around 40 nm with a titania shell of around 2 nm, as we show in the inset of Figure 1b. We have employed TiO_2 shells simply to act as a high refractive index dielectric conformal coating in order to protect the Ag core from the perovskite. Without this coating we would expect the bare Ag nanoparticles to act as recombination sites in the solar cell, and also to become corroded by the halide in the perovskite. The loading of the nanoparticles is suitably low that we
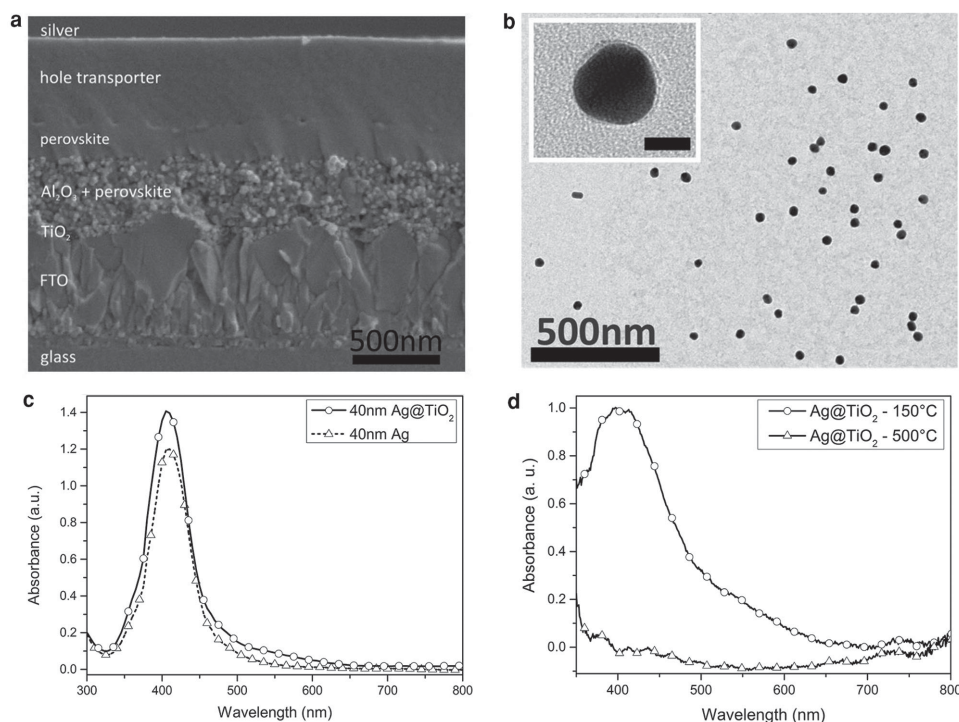
Figure 1. a) SEM cross section of a meso-superstructured solar cell (MSSC). b) TEM image of $Ag@TiO_2$ nanoparticles with 40 nm silver cores and 2 nm titania shells. Inset: magnified image of a single $Ag@TiO_2$ nanoparticle with a 20 nm scale bar. c) Absorbance of silver nanoparticles with (open circles) and without (open triangles) titania shell in ethanol. d) Absorbance of high concentration of $Ag@TiO_2$ NPs in an Al_2O_3 thin film deposited on FTO glass and heated to 150 °C (open circles) and 500 °C (open triangles), respectively. The plasmonic peak of $Ag@TiO_2$ NPs disappears completely upon sintering at 500 °C.

FULL PAPER

do not expect any charge transport between the nanoparticles within the TiO_2 shell.

The Ag@TiO_2 nanoparticles were incorporated into the Al_2O_3 mesoporous layer at different weight ratios of up to 4.4 wt% (Ag@TiO_2/Al_2O_3) while keeping the overall film thickness constant. In Figure 1c we show the absorption spectrum of the Ag NPs with (open circles) and without (open triangles) titania shells in ethanol. A narrow plasmonic peak is observed at around 410 nm for the Ag cores, which is consistent with literature,[58] indicating the good quality of synthesized NPs.

For photovoltaic applications, it is necessary to coat the Ag NPs with a dielectric shell which contributes to chemical and thermal stability and prevents bare Ag NPs from acting as charge carrier recombination centers in the photoactive layer.[41] Generally, thick shells are advantageous due to the increased stability. However, the plasmonic optical near-field only extends to a few tens of nanometers and thus thinner shells around Ag NPs screen less of the plasmonic field as demonstrated in the electromagnetic simulations in Figure S2 (Supporting Information) for a 2 nm and 15 nm thick titania shell. The tradeoff of these two effects imposes an inherent limit for shell thickness. In fact, we observed that the ≈2 nm titania shell used in this study is sufficient for thermal protection as demonstrated in Figure 1d, where the plasmonic peak vanishes upon sintering at 500 °C, precluding Ag@TiO_2 NPs from high temperature processing steps during device fabrication.

It is well reported that the surface atoms in metals start diffusing out at temperatures far below the bulk melting point resulting in a molten liquid surface layer which facilitates the overall melting process.[59,60] This is further influenced by the local surface curvature of the NPs,[61] vapor pressure of the material[54] and substrate support.[62] Thus, shape changes of nanoparticles already occur at low temperatures.[63] Ag NPs in particular, due to a relatively low bulk melting point of 961 °C and high vapor pressure,[54] are very sensitive toward high-temperature steps.[55] Ultimately, this may result in a complete loss of optical properties as we observed here. However, we clearly show that the Ag@TiO_2 NPs in this work remain stable at 150 °C rendering them compatible with our low temperature processing route for the mesoporous alumina perovskite solar cells.[6]

We fabricated devices where none of the heating steps exceeded 150 °C after addition of Ag@TiO_2 NPs into the mesostructure. In **Table 1**, we present the main device performance parameters: short-circuit current density (J_{sc}), open-circuit vol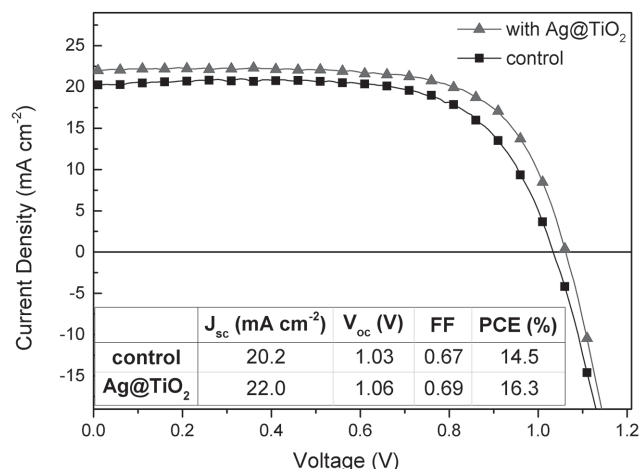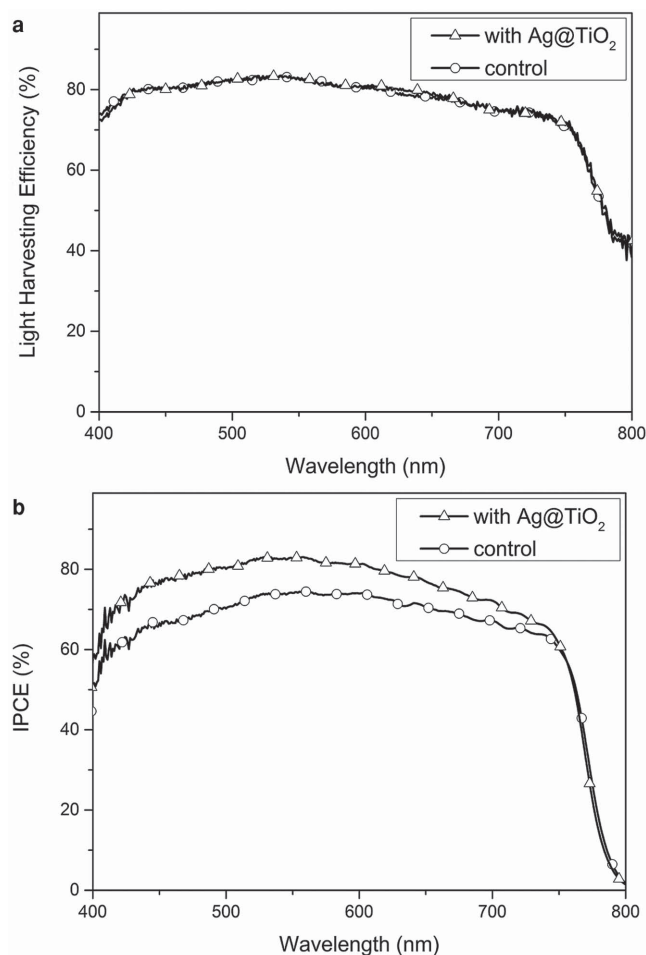tage (V_{oc}), fill factor (FF), and power conversion efficiency (PCE) for different ratios (from 0 to 4.4 wt%) of Ag@TiO_2 NPs mixed into the Al_2O_3 colloid solution. The control devices (0 wt% Ag@TiO_2) exhibited an average PCE of 11.4% ± 1.3%, which is in good agreement with previous reports of a similar device architecture.[6] At optimized Ag@TiO_2 NP concentration (referred to as "Ag@TiO_2 devices" from here on) around 2.2 wt%, we obtained an average PCE of 13.7 ± 1.2%, indicating a 20% enhancement in PCE. This is superior to our previous study[44] where we reported a PCE enhancement by 13%, from 8.4% for the control to 9.5% for the Au@SiO_2 NP containing devices. It should also be noted here that the titania shell, despite being relatively thin, must prevent direct perovskite-silver contact or else we would have observed additional degradation for perovskite solar cells with Ag@TiO_2 (which we do not).

In **Figure 2**, we show the current density–voltage (JV) scans for the best control and Ag@TiO_2 device exhibiting measured PCEs of 14.5% and 16.3%. However, it has now been frequently observed that JV curves can be affected by an anomalous hysteresis. Thus, it is very important to compare at "stabilized conditions" where the efficiency over time is monitored while holding the devices at constant forward bias under AM1.5 illumination. We show the stabilized result in Figure S3 (Supporting Information) where the stabilized power output over time reconfirms the trend for the above JV curves, albeit at a slightly lower efficiency of just under 12% for the control and just over 13% for the Ag@TiO_2 device.[64]

From Table 1, we observed that the average JV scanned power conversion efficiency (PCE) enhancement for the device incorporating Ag@TiO_2 NPs mainly comes from the greatly improved short-circuit photocurrent, whilst the open-circuit voltage (V_{oc}) and fill factor (FF) are only slightly changed. To demonstrate the result of PCE enhancement is reliable, we show data for over 32 devices for both the control and the optimized Ag@TiO_2 devices in Figure S4 (Supporting Information), which reconfirms that the overall increase mainly comes from the J_{sc}.

Table 1. Short-circuit current density (J_{sc}), open-circuit voltage (V_{oc}), fill factor (FF), and power conversion efficiency (PCE) with standard deviations for different concentrations of Ag@TiO_2/Al_2O_3 (wt%) ranging from 0.0 to 4.4 wt% over at least eight devices for each group.

Ag@TiO_2/Al_2O_3 [wt%]	J_{sc} [mA cm^{-2}]	V_{oc} [V]	FF	PCE [%]
0.0	17.3 ± 1.2	1.03 ± 0.03	0.64 ± 0.06	11.4 ± 1.3
1.1	18.0 ± 1.6	1.01 ± 0.01	0.64 ± 0.02	11.6 ± 1.3
2.2	19.7 ± 1.6	1.04 ± 0.01	0.67 ± 0.01	13.7 ± 1.2
3.3	20.2 ± 0.6	1.03 ± 0.02	0.65 ± 0.02	13.5 ± 0.6
4.4	19.9 ± 2.0	1.01 ± 0.03	0.59 ± 0.08	11.8 ± 2.7

	J_{sc} (mA cm^{-2})	V_{oc} (V)	FF	PCE (%)
control	20.2	1.03	0.67	14.5
Ag@TiO_2	22.0	1.06	0.69	16.3

Figure 2. Current density–voltage characteristics for the best control device and optimized Ag@TiO_2 device. The solar cells were measured via scanning from 1.4 V to short circuit at a scan rate of 0.15 V s^{-1}.

Materials
Views
www.MaterialsViews.com

ADVANCED
FUNCTIONAL
MATERIALS
www.afm-journal.de

FULL PAPER

Figure 3. a) Light harvesting efficiency of the photoactive layer for the control (open circles) and Ag@TiO$_2$ (open triangles) devices measured according to Ball et al. b) Incident photon-to-current conversion efficiency (IPCE) for respective devices without (open circles) and with Ag@TiO$_2$ NPs (open triangles).
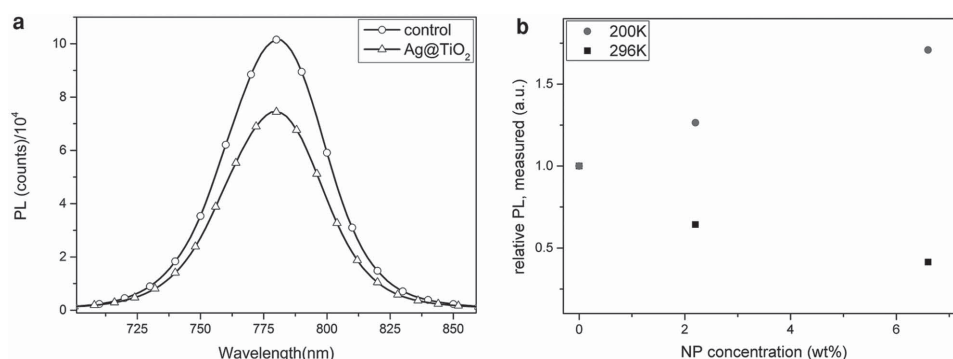
electrodes for dye-sensitized solar cells. They observed higher open-circuit voltages for the cells incorporating the Au@TiO$_2$ nanoparticles, which they assigned to be due to electron accumulation within the Au core, facilitating a negative shift in the quasi Fermi level for electrons in the TiO$_2$.[65] For our study, the V_{oc} variation between devices with and without Ag@TiO$_2$ nanoparticles is small; hence, it is unlikely that this same charging effect is having a strong electronic influence on our cells. We note that the Ag@TiO$_2$ nanoparticles are at low concentration embedded within the mesoporous Al$_2$O$_3$, electronically isolating them from the n-type collection layer. We do note, however, that the silver cores may be accumulating electrons, but this will depend on the precise work function of the silver nanoparticles with respect to the Fermi level with the TiO$_2$ shells.

To rule out the possibility that the enhanced photocurrent is induced by the TiO$_2$ shell itself rather than the silver core, we ran a control experiment by using similarly sized pure titania beads mixed into the Al$_2$O$_3$ scaffold at ratios equivalent to the molarity of the Ag@TiO$_2$ particles. As we show in Figure S5 (Supporting Information), there is no significant difference between control devices and devices incorporating titania beads, leaving us to conclude that the silver core is essential for the observed enhancement, as we previously saw for the silica-coated gold nanoparticles.[44]

We further studied the optical effect of the Ag@TiO$_2$ NPs on device performance through measuring the light harvesting efficiency of full perovskite solar cells with silver back contacts.[6,44] In **Figure 3**a, we show UV–vis spectra (obtained with an integrating sphere) of control and Ag@TiO$_2$ devices exhibiting no significant difference. As the next step, we measured the incident photon-to-current conversion efficiency (IPCE) (see Figure 3b). The Ag@TiO$_2$ devices outperform the control devices as expected from the short-circuit current density in Table 1. However, the enhancement is broadband (between 400 and 750 nm) rather than focused around any sharp peak, or a specific enhancing of the red edge, which can therefore not be attributed to the optical spectrum of the Ag@TiO$_2$ NPs.

To understand the photocurrent enhancement mechanism in more detail, we studied the photoluminescence (PL) at room temperature of 296 K (**Figure 4**a) and observed a clear quenching of the steady-state PL for the Ag@TiO$_2$ containing films. Figure 4b shows the integrated PL data at room

Choi et al. have previously investigated the electronic differences between employing TiO$_2$ versus SiO$_2$ as the shell material for metal nanoparticles embedded within mesoporous TiO$_2$

Figure 4. a) Steady-state photoluminescence (PL) at room temperature of 296 K for control (open circles) and Ag@TiO$_2$ NP (open triangles) containing films. b) Integrated PL at 296 K and 200 K for three different film samples with 0, 2.2, and 6.6 wt% Ag@TiO$_2$. The values were normalized to "1" for the samples without nanoparticles.

temperature with 0, 2.2, and 6.6 wt% Ag@TiO$_2$ concentration for 200 and 296 K (room temperature). The data were normalized at "1" for the samples without nanoparticles.

Clearly, the quenching at room temperature is even more pronounced for higher NP concentration. Interestingly, this trend reverses when measuring the same samples at 200 K. Here, the samples with Ag@TiO$_2$ exhibit a PL enhancement which is in line with our previous work,[44] where we postulated that the photocurrent enhancement in the presence of plasmonic NPs was due to enhancement in the exciton ionization rate. However, our previous interpretation relied on the stated assumption that light emission mainly originates from exciton decay, and not from the recombination of free charges. It is now well recognized that free charges recombine radiatively in organic–inorganic metal halide perovskites.[66] Hence, monitoring the temperature dependence of the PL intensity will not deliver an estimation of the exciton binding energy. Furthermore, there is growing evidence that the exciton binding energy in the CH$_3$NH$_3$PbI$_3$ perovskite at room temperature is on the order of or less than 10 meV.[67,68] Hence, we do not expect small changes to the exciton binding to result in significant changes of photocurrent generation in the solar cell, since the free charge population should dominate. Therefore, an accurate understanding of the mechanism for photocurrent enhancement in perovskite solar cells with the addition of metallic nanoparticles is still required.

At first sight, the reduced PL at room temperature would appear to be a disadvantage for a solar cell absorber material since it indicates enhanced nonradiative decay channels.[69] However, in order to understand both the photocurrent enhancement and photoluminescence quenching we propose a theory outlined in more detail below. In short, the Ag@TiO$_2$ nanoparticles may act as antennas for the excitonic dipoles. Photons emitted from exciton decay would then have an extended optical pathlength because they are attracted toward the highly polarizable Ag NPs which are lying in the plane of the perovskite film. By this means the reabsorption from reemitted light is enhanced, in essence enabling photon recycling with a much greater efficiency.[67–69] We note that we expect this same mechanism has driven the enhanced photocurrent in perovskite solar cells which we previously observed with the addition of Au@SiO$_2$ nanoparticles.

3. Interpretation of Temperature-Dependent Photoluminescence

In this section, we give an interpretation for the temperature-dependent photoluminescence in the presence of highly polarizable metal nanoparticles.

We take two factors into account for the presence of metallic nanoparticles:

1. high polarizability of the nanoparticles[70] increasing exciton radiation probability,[71,72] and
2. change in exciton radiation geometry due to the presence of strong dipoles, as we illustrate in **Figure 5**, which may result in either an increase or decrease of radiation reabsorption.

The first factor simply means that exciton radiation can be significantly increased in the vicinity of highly polarizable metal nanoparticles.[72]

The second factor takes into account that the radiation path from an exciton decay can now be deflected through neighboring NPs, i.e., effectively increasing the optical pathway, and thus making reabsorption more likely, enabling multiple chances for the photon energy to generate current.

Thus, reabsorption of exciton radiation within the perovskite film is increased in the presence of the nanoparticles.

These assumptions are sufficient to provide a model for temperature-dependent PL data which is outlined in full detail in the Supporting Information. Here, in the interest of brevity, we present one of the main conclusions of our calculations, i.e., the relative ratio of the external PL intensity, I_{Rel}, with and without nanoparticles

$$I_{Rel} = \frac{n_{ex} R_1 \exp(-\alpha\, l_1)}{n_{ex} R_0 \exp(-\alpha\, l_0)} = (1 + k_0\, n_{NP}) \exp(-\alpha\, k_1\, n_{NP}\, l_0) \qquad (1)$$
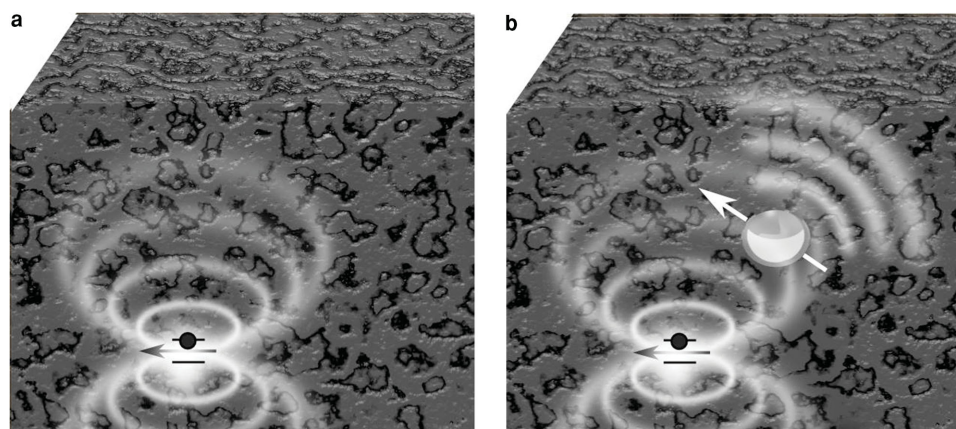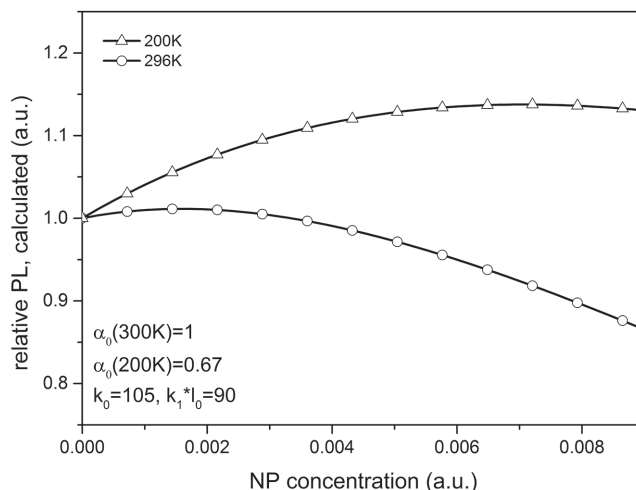

Figure 5. Proposed mechanism within a perovskite film. a) Thin solid lines (in white) show the electric field distribution around the exciton dipole moment d_{exc} (illustrated by the arrow). b) Due to the high polarizability the silver nanoparticles acquire significant dipole moments D (illustrated by the white arrow at the top), which facilitate radiative decay of the exciton through the NPs. This means that the light gets redirected onto a longer optical pathlength (shown by the additional field lines emitted from the Ag NP).

www.MaterialsViews.com

ADVANCED
FUNCTIONAL
MATERIALS
www.afm-journal.de

FULL PAPER
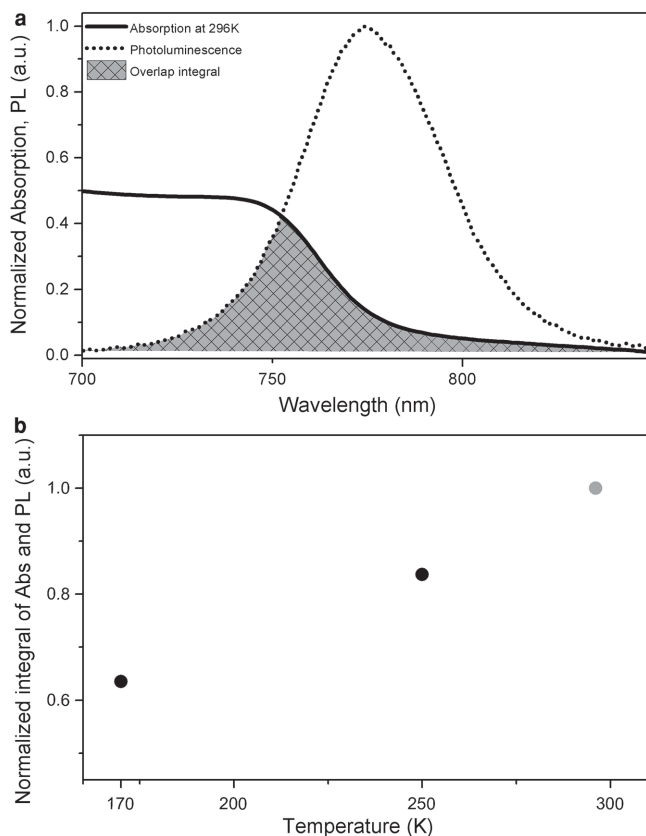
Figure 6. a) Absorption and PL spectra of perovskite films at room temperature of 296 K. The patterned overlap area is used to calculate the integral of the product of absorption and PL spectra. b) Overlap integral of the product of the absorption and PL spectrum at room temperature as calculated from (a). Accordingly, we performed the same calculation for 170 and 250 K absorption spectra, as measured by D'Innocenzo et al. The scale is normalized to the room temperature value.

Figure 7. Simulation results for relative external PL for perovskite films with Ag@TiO$_2$ NPs at T = 296 K (open circle) and T = 200 K (open triangle) obtained by using Equation (1). Model parameters used for fitting are k_0 = 105 and $k_1 \times l_0$ = 90, α_0(200 K) = 0.67, α_0(296 K) = 1.0.

where n_{ex} is the exciton concentration, R_0 is the exciton radiative decay rate, $\alpha(T)$ is the temperature-dependent absorption coefficient of the perovskite absorber, l_0 is an effective optical pathlength for outgoing radiation in neat perovskite films, l_1 is an effective optical pathlength for outgoing radiation in perovskite films with nanoparticles, k_0 and k_1 are constants defining the increase in the radiation rate and in effective optical path, respectively, and n_{NP} is the NP concentration. This expression relates the relative emitted PL intensity with the NP concentration where k_0 and $k_1 \times l_0$ are used as fitting parameters. It is noteworthy that the only experimental parameter in this equation is the temperature-dependent absorption coefficient $\alpha(T)$. Absorption and PL spectra for perovskite films at 170, 250, and 296 K were reported by D'Innocenzo et al.[73] Furthermore, the overlap area between absorption and PL is a measure for how likely an emitted photon gets reabsorbed by the perovskite film. We illustrate this in **Figure 6**a where we show the overlap area between the measured absorption and PL spectrum of the perovskite absorber at room temperature. Thus, we can calculate the normalized integral of the product of absorption and PL over temperatures of 170, 250, and 296 K as we present in Figure 6b. From this, it is clear that as the temperature increases the overlap area between absorption

and PL increases as well, implying enhanced reabsorption of emitted photons.

Now we can use k_0 and $k_1 \times l_0$ in Equation (1) as fitting parameters to model experimental PL data at different temperatures T. This means the fitting parameters are arbitrary but fixed for the different temperatures and only $\alpha(T)$ varies according to the experimental data from Figure 6b. In **Figure 7** we show typical simulation results for the PL data at 296 and 200 K over nanoparticle concentration n_{NP}.

The simulation data at room temperature (296 K) shows initially a small PL increase with very low concentrations, but a predominant quenching as the NP concentration increases.

This trend is reverted for 200 K, with the peak in external PL occurring at a much higher NP concentration. This is precisely the trend observed for the experimental data in Figure 4b. Therefore, the proposed model provides a qualitative understanding of the experimental trend.

We note that the relative enhancement or reduction in external PL with temperature is entirely accountable for changes to the reabsorption of light following emissive decay of the electrons and holes. The trends do not require any increase in the nonradiative decay pathways for electrons and holes, and are thus consistent with the enhanced photocurrent observed in the solar cells.

4. Conclusion

We embedded thermally sensitive core–shell silver-titania nanoparticles into perovskite solar cells with processing temperatures below 150 °C. This may be of particular interest for nonspherical nanoparticles which are notoriously hard to stabilize against temperature-induced shape changes. We observed an average efficiency increase by ≈20% from 11.4% ± 1.3% for control to 13.7% ± 1.2% for optimized Ag@TiO$_2$ NP containing devices. The enhancement is mainly due to increased short-circuit current density. In contrast to expectations, despite the systematic increase in photocurrent, the

FULL PAPER

isolated perovskite films exhibit a quenching of the externally measured photoluminescence which would generally indicate an increase in disadvantageous nonradiative decay pathways in the solar cells. We propose a theory whereby the radiative dipoles of the excitons (electron–hole pairs shortly proceeding recombination) within the perovskite film interacting with the dipoles of the metal nanoparticles. This interaction results in enhanced (faster) radiative decay but also partially guides the reemitted light into the plane of the film. The first mechanism increases the external photoluminescence, but the second mechanism reduces the external photoluminescence through increasing the reabsorption of emitted light within the perovskite film. This whole process can be considered a novel method to enhance photon recycling within a photovoltaic device. We develop a theoretical model based on this concept which reproduces the temperature-dependent PL data and explains both an increase and reduction in PL intensity with increasing nanoparticle concentration at low and high temperatures, respectively. This study helps to broaden our understanding of the impact of plasmonic materials within perovskite semiconductors, and subsequent optoelectronic applications. Once the external PL efficiency of the perovskite films in complete solar cells approaches 100%, this plasmonic scheme may help perovskite solar cells reach close to the Shockley–Queisser limit. The mechanism we have proposed may prove to be general to all PV devices incorporating metal nanoparticles, but further work to corroborate this is required.

5. Experimental Section

Materials: Ethylene glycol (anhydrous, 99.8%), polyvinylpyrrolidone (PVP, average M_W = 10 000), silver nitrate (AgNO$_3$, >99%), and titanium isopropoxide (TPO, 97%) were purchased from Sigma-Aldrich. Ammonium hydroxide (NH$_4$OH, 29%) was obtained from Fisher Chemical. Acetone (ACS grade) and ethanol (absolute, anhydrous) were purchased from Pharmco-Aaper. All chemicals were used as received without further purification.

Synthesis and Characterization of Ag@TiO$_2$ NPs: 30–40 nm Ag NPs were synthesized by a polyol method, according to a reported procedure with slight modifications.[42] Typically, 0.5 g of PVP-10 was added into 25 mL of ethylene glycol, and the mixture was vigorously stirred until PVP-10 was fully dissolved. 17 mg of AgNO$_3$ was then added to the solution under stirring. After AgNO$_3$ was fully dissolved, the mixture was heated to 120 °C from room temperature and kept at that temperature for 1 h under stirring. The native Ag NPs were separated from ethylene glycol by adding 200 mL of acetone, followed by centrifugation. The precipitate was further redispersed into ethanol and centrifuged again. The final precipitate was redispersed into 20 mL ethanol solution containing 0.4% ammonia. The suspension was then sonicated for 30 min using an ultrasonication bath before the shell addition step. In order to grow a 2–3 nm TiO$_2$ shell, 2 mL of 20.3 × 10^{-3} M TPO in ethanol was injected into the above Ag NPs suspension under vigorous stirring. After stirring for 24 h in the dark, Ag@TiO$_2$ NPs were cleaned by centrifugation and redispersion in ethanol.

Device Fabrication: The low-temperature perovskite device fabrication was reported elsewhere.[6] In short, fluorine-doped tin oxide patterned glass (Pilkington TEC 7, 7 Ω □$^{-1}$) was cleaned sequentially in Hellmanex, Milli-Q water, acetone, ethanol and oxygen plasma etching. A TiO$_2$ compact layer was deposited by spin coating a 0.253 M titanium isopropoxide precursor (diluted in a mildly acidic anhydrous ethanol solution) at a speed of 2000 rpm for 60 s followed by sintering at 500 °C for 45 min. After cooling to room temperature an Al$_2$O$_3$ scaffold was

spin coated at 2500 rpm for 45 s from a colloidal dispersion of <50 nm Al$_2$O$_3$ nanoparticles (Sigma-Aldrich, product number 702129), followed by drying at 150 °C for 30 min. Throughout all experiments the scaffold thickness was kept constant at about 350 nm by diluting the Al$_2$O$_3$ NPs with ethanol in a 1:2 volume ratio. Silver nanoparticles dispersed in ethanol were incorporated into the Al$_2$O$_3$ scaffold by replacing appropriate amounts of ethanol used for the Al$_2$O$_3$ dilution such that the weight ratio of Ag@TiO$_2$/Al$_2$O$_3$ ranged from 1.1 to 4.4 wt%. All dispersions were put in an ultrasonic bath for at least 10 min to ensure optimal mixing. In the next step a perovskite solution (40 wt% of methylammonium iodide (CH$_3$NH$_3$I) and lead(II) chloride (PbCl$_2$) in a 3:1 molar ratio in dimethylformamide (DMF)) was spin coated at 2000 rpm for 45 s and then heated at 100 °C for 90 min. Upon cooling to room temperature the hole-transporting layer was deposited by spin coating 2,2′,7,7′-tetrakis-(N,N-di-p-methoxyphenylamine)9,9′-spirobifluorene (Spiro-OMeTAD) at 2000 rpm for 45 s. The Spiro-OMeTAD concentration was 80 × 10^{-3} M in chlorobenzene with an added 30 mol% lithium bis(trifluoromethanesulfonyl)imide (Li-TFSI) and 80 mol% *tert*-butylpyridine (tBP). The devices were then left in a light-tight desiccator overnight. Finally, 150 nm thick silver electrodes were evaporated onto the devices through a shadow mask.

Device Characterization: Current–voltage characteristics were measured with a Keithley 2400 under AM 1.5G 100 mW cm^{-2} simulated sunlight (Abet Technologies Sun 2000) calibrated against an NREL certified KG5 filtered silicon reference diode. The solar cells were masked with a square aperture defining an active area of typically 0.0625 cm^2 and measured in a light-tight sample holder. Incident photon-to-current conversion efficiency (IPCE) was measured via Fourier-transform photocurrent spectroscopy. The measurement system consisted of a Bruker Vertex 80v Fourier transform spectrometer combined with a Stanford Research SR570 current preamplifier, Thurlby Thandar Instruments PL303QMD power supply, and custom-built control electronics. The spectrometer was configured with a tungsten–halogen light source and CaF$_2$ beamsplitter. The spectra were calibrated against measurements taken with the same system on a reference silicon solar cell with a known External Quantum Efficiency. The BK7 filtered reference silicon solar cell was calibrated at the National Renewable Energy Laboratory (NREL). All solar cells were masked with a metal aperture to define the active area of 0.0625 cm^2.

UV–Vis Spectra: Samples for optical UV–vis measurements were fabricated in the same way as the devices described above. A Carry 300 Bio (Agilent Technologies) with an integrating sphere accessory was used to determine the absorptance of the active layer in the full device. The experimental details are published elsewhere.[6]

Steady-State PL Spectra: Time-integrated photoluminescence (PL) spectra of devices without spiro-OMeTAD and top electrodes were acquired using a time-correlated single photon counting (TCSPC) setup (FluoTime 300, PicoQuant GmbH). Samples were photoexcited through the glass using a 507 nm laser head (LDH-P-C-510, PicoQuant GmbH) with pulse duration of 117 ps, fluence of ≈0.03 nJ cm^{-2}, and a repetition rate of 2 MHz. Eight samples were measured for each experimental parameter and the time-integrated spectra were presented. Low-temperature measurements were carried out using an Oxford Instruments OptistatDN cryostat with a specialized fitting for the TCSPC setup.

Simulations: Simulations of the electromagnetic field were conducted with the software package OpenMaXwell,[74] i.e., a semianalytical Maxwell solver using multiple multipoles comprised of exact solutions of the Maxwell equations to model the overall time-harmonic electromagnetic field. The calculations assumed plane wave excitation (at dipole resonance) with the following refractive indices: 1.76 for alumina, 2.5 for titania, 2.55 for perovskite,[75,76] and n_{silver} from Johnson and Christy.[77]

Supporting Information

Supporting Information is available from the Wiley Online Library or from the author.

www.MaterialsViews.com

ADVANCED
FUNCTIONAL
MATERIALS
www.afm-journal.de

FULL PAPER

Acknowledgements

[1] D. Weber, *Z. Naturforsch. B* **1978**, *33*, 1443.

[2] A. Kojima, K. Teshima, Y. Shirai, T. Miyasaka, *J. Am. Chem. Soc.* **2009**, *131*, 6050.

[3] J. H. Im, C. R. Lee, J. W. Lee, S. W. Park, N. G. Park, *Nanoscale* **2011**, *3*, 4088.

[4] H. S. Kim, C. R. Lee, J. H. Im, K. B. Lee, T. Moehl, A. Marchioro, S. J. Moon, R. Humphry-Baker, J. H. Yum, J. E. Moser, M. Gratzel, N. G. Park, *Sci. Rep.* **2012**, *2*, 591.

[5] M. M. Lee, J. Teuscher, T. Miyasaka, T. N. Murakami, H. J. Snaith, *Science* **2012**, *338*, 643.

[6] J. M. Ball, M. M. Lee, A. Hey, H. J. Snaith, *Energy Environ. Sci.* **2013**, *6*, 1739.

[7] L. Etgar, P. Gao, Z. Xue, Q. Peng, A. K. Chandiran, B. Liu, M. K. Nazeeruddin, M. Gratzel, *J. Am. Chem. Soc.* **2012**, *134*, 17396.

[8] C. Wehrenfennig, M. Z. Liu, H. J. Snaith, M. B. Johnston, L. M. Herz, *Energy Environ. Sci.* **2014**, *7*, 2269.

[9] S. D. Stranks, G. E. Eperon, G. Grancini, C. Menelaou, M. J. Alcocer, T. Leijtens, L. M. Herz, A. Petrozza, H. J. Snaith, *Science* **2013**, *342*, 341.

[10] G. C. Xing, N. Mathews, S. Y. Sun, S. S. Lim, Y. M. Lam, M. Gratzel, S. Mhaisalkar, T. C. Sum, *Science* **2013**, *342*, 344.

[11] E. Edri, S. Kirmayer, S. Mukhopadhyay, K. Gartsman, G. Hodes, D. Cahen, *Nat. Commun.* **2014**, *5*, 3461.

[12] T. Baikie, Y. N. Fang, J. M. Kadro, M. Schreyer, F. X. Wei, S. G. Mhaisalkar, M. Graetzel, T. J. White, *J. Mater. Chem. A* **2013**, *1*, 5628.

[13] J. Burschka, N. Pellet, S. J. Moon, R. Humphry-Baker, P. Gao, M. K. Nazeeruddin, M. Gratzel, *Nature* **2013**, *499*, 316.

[14] M. Z. Liu, M. B. Johnston, H. J. Snaith, *Nature* **2013**, *501*, 395.

[15] J. H. Rhee, C. C. Chung, E. W. G. Diau, *NPG Asia Mater.* **2013**, *5*, e68.

[16] H. J. Snaith, *J. Phys. Chem. Lett.* **2013**, *4*, 3623.

[17] K. Wojciechowski, M. Saliba, T. Leijtens, A. Abate, H. Snaith, *Energy Environ. Sci.* **2013**, *7*, 1142.

[18] A. Abate, M. Saliba, D. J. Hollman, S. D. Stranks, K. Wojciechowski, R. Avolio, G. Grancini, A. Petrozza, H. J. Snaith, *Nano Lett.* **2014**, *14*, 3247.

[19] B. Conings, L. Baeten, C. De Dobbelaere, J. D'Haen, J. Manca, H. G. Boyen, *Adv. Mater.* **2014**, *26*, 2041.

[20] H. Dong, X. Guo, W. Li, L. Wang, *RSC Adv.* **2014**, *4*, 60131.

[21] G. E. Eperon, V. M. Burlakov, P. Docampo, A. Goriely, H. J. Snaith, *Adv. Funct. Mater.* **2014**, *24*, 151.

[22] J. H. Im, I. H. Jang, N. Pellet, M. Gratzel, N. G. Park, *Nat. Nanotechnol.* **2014**, *9*, 927.

[23] N. J. Jeon, J. H. Noh, Y. C. Kim, W. S. Yang, S. Ryu, S. Il Seol, *Nat. Mater.* **2014**, *13*, 897.

[24] J.-W. Lee, D.-J. Seol, A.-N. Cho, N.-G. Park, *Adv. Mater.* **2014**, *26*, 4991.

[25] M. R. Leyden, L. K. Ono, S. R. Raga, Y. Kato, S. Wang, Y. Qi, *J. Mater. Chem. A* **2014**, *2*, 18742.

[26] O. Malinkiewicz, A. Yella, Y. H. Lee, G. M. Espallargas, M. Graetzel, M. K. Nazeeruddin, H. J. Bolink, *Nat. Photon* **2014**, *8*, 128.

[27] S. Paek, N. Cho, H. Choi, H. Jeong, J. S. Lim, J.-Y. Hwang, J. K. Lee, J. Ko, *J. Phys. Chem. C* **2014**, *118*, 25899.

[28] C. Roldan-Carmona, O. Malinkiewicz, A. Soriano, G. Minguez Espallargas, A. Garcia, P. Reinecke, T. Kroyer, M. I. Dar, M. K. Nazeeruddin, H. J. Bolink, *Energy Environ. Sci.* **2014**, *7*, 994.

[29] M. Saliba, K. W. Tan, H. Sai, D. T. Moore, T. Scott, W. Zhang, L. A. Estroff, U. Wiesner, H. J. Snaith, *J. Phys. Chem. C* **2014**, *118*, 17171.

[30] K. W. Tan, D. T. Moore, M. Saliba, H. Sai, L. A. Estroff, T. Hanrath, H. J. Snaith, U. Wiesner, *ACS Nano* **2014**, *8*, 4730.

[31] J. T. Wang, J. M. Ball, E. M. Barea, A. Abate, J. A. Alexander-Webber, J. Huang, M. Saliba, I. Mora-Sero, J. Bisquert, H. J. Snaith, R. J. Nicholas, *Nano Lett.* **2014**, *14*, 724.

[32] J. You, J. Yang, Z. Hong, T.-B. Song, L. Meng, Y. Liu, C. Jiang, H. Zhou, W.-H. Chang, G. Li, Y. Yang, *Appl. Phys. Lett.* **2014**, *105*, 183902.

[33] J. H. Kim, P. W. Liang, S. T. Williams, N. Cho, C. C. Chueh, M. S. Glaz, D. S. Ginger, A. K. Jen, *Adv. Mater.* **2015**, *27*, 695.

[34] W. Nie, H. Tsai, R. Asadpour, J.-C. Blancon, A. J. Neukirch, G. Gupta, J. J. Crochet, M. Chhowalla, S. Tretiak, M. A. Alam, H.-L. Wang, A. D. Mohite, *Science* **2015**, *347*, 522.

[35] W. Y. Nie, H. H. Tsai, R. Asadpour, J. C. Blancon, A. J. Neukirch, G. Gupta, J. J. Crochet, M. Chhowalla, S. Tretiak, M. A. Alam, H. L. Wang, A. D. Mohite, *Science* **2015**, *347*, 522.

[36] D. Shi, V. Adinolfi, R. Comin, M. J. Yuan, E. Alarousu, A. Buin, Y. Chen, S. Hoogland, A. Rothenberger, K. Katsiev, Y. Losovyj, X. Zhang, P. A. Dowben, O. F. Mohammed, E. H. Sargent, O. M. Bakr, *Science* **2015**, *347*, 519.

[37] D. M. Schaadt, B. Feng, E. T. Yu, *Appl. Phys. Lett.* **2005**, 86.

[38] H. A. Atwater, A. Polman, *Nat. Mater.* **2010**, *9*, 205.

[39] J. Yang, J. B. You, C. C. Chen, W. C. Hsu, H. R. Tan, X. W. Zhang, Z. R. Hong, Y. Yang, *ACS Nano* **2011**, *5*, 6210.

[40] X. H. Li, W. C. H. Choy, L. J. Huo, F. X. Xie, W. E. I. Sha, B. F. Ding, X. Guo, Y. F. Li, J. H. Hou, J. B. You, Y. Yang, *Adv. Mater.* **2012**, *24*, 3046.

[41] M. D. Brown, T. Suteewong, R. S. Kumar, V. D'Innocenzo, A. Petrozza, M. M. Lee, U. Wiesner, H. J. Snaith, *Nano Lett.* **2011**, *11*, 438.

[42] J. F. Qi, X. N. Dang, P. T. Hammond, A. M. Belcher, *ACS Nano* **2011**, *5*, 7108.

[43] P. Reineck, G. P. Lee, D. Brick, M. Karg, P. Mulvaney, U. Bach, *Adv. Mater.* **2012**, *24*, 4750.

[44] W. Zhang, M. Saliba, S. D. Stranks, Y. Sun, X. Shi, U. Wiesner, H. J. Snaith, *Nano Lett.* **2013**, *13*, 4505.

[45] J. N. Anker, W. P. Hall, O. Lyandres, N. C. Shah, J. Zhao, R. P. Van Duyne, *Nat. Mater.* **2008**, *7*, 442.

[46] J.-S. Huang, T. Feichtner, P. Biagioni, B. Hecht, *Nano Lett.* **2009**, *9*, 1897.

[47] T. Ergin, N. Stenger, P. Brenner, J. B. Pendry, M. Wegener, *Science* **2010**, *328*, 337.

[48] M. Hentschel, M. Saliba, R. Vogelgesang, H. Giessen, A. P. Alivisatos, N. Liu, *Nano Lett.* **2010**, *10*, 2721.

[49] N. Liu, M. Hentschel, T. Weiss, A. P. Alivisatos, H. Giessen, *Science* **2011**, *332*, 1407.

[50] M. Rycenga, C. M. Cobley, J. Zeng, W. Y. Li, C. H. Moran, Q. Zhang, D. Qin, Y. N. Xia, *Chem. Rev.* **2011**, *111*, 3669.

[51] M. I. Stockman, *Opt. Express* **2011**, *19*, 22029.

[52] T. C. Deivaraj, N. L. Lala, J. Y. Lee, *J. Colloid Interface Sci.* **2005**, *289*, 402.

[53] J. G. Lee, J. Lee, T. Tanaka, H. Mori, *Phys. Rev. Lett.* **2006**, *96*, 075504.

[54] Y. Khalavka, C. Ohm, L. Sun, F. Banhart, C. Sonnichsen, *J. Phys. Chem. C* **2007**, *111*, 12886.

[55] R.-X. Dong, C.-C. Chou, J.-J. Lin, *J. Mater. Chem.* **2009**, *19*, 2184.

[56] P. Ramasamy, D. M. Seo, S. H. Kim, J. Kim, *J. Mater. Chem.* **2012**, *22*, 11651.

[57] M. A. Asoro, D. Kovar, P. J. Ferreira, *ACS Nano* **2013**, *7*, 7844.

[58] C. F. Bohren, D. R. Huffman, *Absorption and Scattering of Light by Small Particles*, Wiley, New York **2008**.

[59] P. Buffat, J. P. Borel, *Phys. Rev. A* **1976**, *13*, 2287.

[60] P. R. Couchman, W. A. Jesser, *Nature* **1977**, *269*, 481.

[61] R. Kofman, P. Cheyssac, A. Aouaj, Y. Lereah, G. Deutscher, T. Bendavid, J. M. Penisson, A. Bourret, *Surf. Sci.* **1994**, *303*, 231.

[62] K. K. Nanda, *Pramana J. Phys.* **2009**, *72*, 617.

[63] H. Petrova, J. Perez Juste, I. Pastoriza-Santos, G. V. Hartland, L. M. Liz-Marzan, P. Mulvaney, *Phys. Chem. Chem. Phys.* **2006**, *8*, 814.

[64] H. J. Snaith, A. Abate, J. M. Ball, G. E. Eperon, T. Leijtens, N. K. Noel, S. D. Stranks, J. T. W. Wang, K. Wojciechowski, W. Zhang, *J. Phys. Chem. Lett.* **2014**, *5*, 1511.

[65] H. Choi, W. T. Chen, P. V. Kamat, *ACS Nano* **2012**, *6*, 4418.

[66] F. Deschler, M. Price, S. Pathak, L. E. Klintberg, D. D. Jarausch, R. Higler, S. Huttner, T. Leijtens, S. D. Stranks, H. J. Snaith, M. Atature, R. T. Phillips, R. H. Friend, *J. Phys. Chem. Lett.* **2014**, *5*, 1421.

[67] J. Even, L. Pedesseau, C. Katan, *J. Phys. Chem. C* **2014**, *118*, 11566.

[68] Q. Q. Lin, A. Armin, R. C. R. Nagiri, P. L. Burn, P. Meredith, *Nat. Photonics* **2015**, *9*, 106.

[69] K. Tvingstedt, O. Malinkiewicz, A. Baumann, C. Deibel, H. J. Snaith, V. Dyakonov, H. J. Bolink, *Sci. Rep.* **2014**, *4*.

[70] P. M. Bendix, L. Jauffred, K. Norregaard, L. B. Oddershede, *IEEE J. Sel. Topics Quantum Electron.* **2014**, *20*.

[71] A. Hatef, S. M. Sadeghi, M. R. Singh, *Nanotechnology* **2012**, *23*, 205203.

[72] C. C. D. Wang, W. C. H. Choy, C. H. Duan, D. D. S. Fung, W. E. I. Sha, F. X. Xie, F. Huang, Y. Cao, *J. Mater. Chem.* **2012**, *22*, 1206.

[73] V. D'Innocenzo, G. Grancini, M. J. Alcocer, A. R. Kandada, S. D. Stranks, M. M. Lee, G. Lanzani, H. J. Snaith, A. Petrozza, *Nat. Commun.* **2014**, *5*, 3586.

[74] C. Hafner, *Post-Modern Electromagnetics: Using Intelligent Maxwell Solvers*, Wiley, New York **1999**.

[75] M. Hirasawa, T. Ishihara, T. Goto, K. Uchida, N. Miura, *Physica B* **1994**, *201*, 427.

[76] K. Tanaka, T. Takahashi, T. Ban, T. Kondo, K. Uchida, N. Miura, *Solid State Commun.* **2003**, *127*, 619.

[77] P. B. Johnson, R. W. Christy, *Phys. Rev. B: Condens. Matter* **1972**, *6*, 4370.